States Modulation in Graphene Nanoribbons through Metal Contacts

Chloé Archambault and Alain Rochefort*

Engineering Physics Department and Regroupement Québécois sur les Matériaux de Pointe (RQMP), École Polytechnique de Montréal, Montréal, Québec H3C 3A7, Canada

ABSTRACT We are reporting the results of density functional calculations of the electronic structure of finite graphene nanoribbons adsorbed on Au, Pd, and Ti electrodes. While the interaction of nanoribbons with the Au contact is more characteristic of a physisorbed state, the adsorption of Pd and Ti involves much stronger state mixing as in chemisorption. Metal-induced gap states, which can potentially short-circuit the device, are clearly revealed for the first time, allowing us to evaluate their penetration length. The evanescence of MIGS is primarily governed by the band gap of the nanoribbon, and we can estimate an acceptable minimal length for an effective transport channel to a few nanometers. Different impacts of the presence of metal-induced gap states on the properties of graphene nanoribbons are discussed in terms of charge transfer and electrostatics.

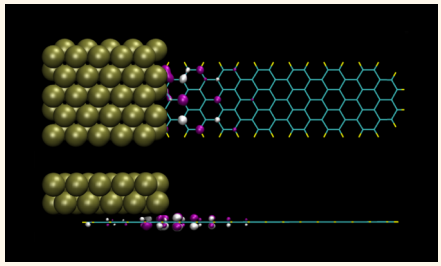

KEYWORDS: graphene nanoribbons · metal contacts · metal-induced gap states · charge transfer · density functional theory · electronic structure

Ever since its discovery, the interest in graphene and its possible applications in electronics has grown. Graphene nanoribbons (GNRs), because of their semiconducting behavior and their atomic thickness, appear as very promising candidates for future miniaturized electronic devices. Beyond its exceptional electrical properties, its perfect two-dimensional structure makes graphene particularly appealing since it could be more easily patternable by current microfabrication techniques. On the other hand, most of our electronic devices such as transistors do not require a semimetal material as graphene but rather a semiconductor. Fortunately, the engineering of graphene into nanoribbons opens a band gap that depends on the chirality.[1−3] This band gap is predicted to be the largest for armchair GNRs, for which we are expecting large On/Off ratios. Following recent experimental progress, GNRs can now be created with a nearly atomic precision.[4]

Hence, transistors made of nanoribbons have already been reported.[5−8] According to Schwierz,[9] one major advantage of using GNRs is related to their low dimensionality, which makes them less subject to short channel effects, such as threshold voltage roll-off and drain-induced barrier lowering, responsible for degraded characteristics.[10] This characteristic sounds quite appealing to sustain a constant miniaturization, but this does not consider an additional but crucial component of any working devices, which are the metallic contacts. The influence of these contacts becomes even more critical when scaling down as the channel length becomes comparable to the length over which contact-induced effects span. If not taken into account, the latter can become dominant and lead to data misinterpretation.[11] In general, the electronic description of the interaction between GNRs and electrodes is often neglected even though this may play a critical role in the final device performance. For example, the charge doping by long-range charge transfer[12,13] and by metal-induced gap states (MIGS)[14] has already been observed for different graphene/metal systems. MIGS could dramatically affect the On/Off ratio, especially in short devices. As suggested by quantum calculations, similar effects are also anticipated in GNRs.[15−18]

MIGS are exponentially decaying states that arise from the complex band structure of a semiconductor connected to a metal.[19] In other words, they are Bloch states derived from the valence and conduction bands with a complex wave vector such that the density decays as $e^{-x/L}$. The decay length L is proportional to $1/q$, q being the imaginary part of the wave vector, which is only

* Address correspondence to alain.rochefort@polymtl.ca.

Received for review March 18, 2013 and accepted May 15, 2013.

Published online May 15, 2013
10.1021/nn401357p

nonzero inside the gap. For a simple one-dimensional semiconductor with band gap E_g and lattice constant a, the decay length of a MIGS with energy E measured from the middle on the gap is[20]

$$L = \frac{\pi\hbar^2}{2m_e a}\left[\left(\frac{E_g}{2}+E\right)\left(\frac{E_g}{2}-E\right)\right]^{-1/2} \quad (1)$$

As indicated in eq 1, L diverges at the limits of the gap where the imaginary part of the wave vector vanishes. Note also that L is minimal for MIGS located in the middle of the gap, where

$$L_{min} = \frac{\pi\hbar^2}{E_g m_e a} \quad (2)$$

In this paper, we have calculated, with the help of density functional theory (DFT), the electronic structure of finite armchair GNRs adsorbed on three different metallic contacts (Au(111), Pd(111), and Ti(0001)), as illustrated in Figure 1(b). The GNRs are denoted $M \times N$ where M (respectively N) is the number of armchair (respectively zigzag) rows along the width (respectively the length) of the nanoribbon, as shown in Figure 1(a), where one armchair and one zigzag row have been highlighted. This approach allows us to take into account finite size effects[21,22] that should not be neglected when dealing with very small devices.

A direct observation of MIGS extending over 1−2 nm into the channel is reported for the first time using a first-principles approach. The calculated penetration length strongly depends on the atomic structure of the GNR through the band-gap modulations. MIGS lead to an evanescent charge distribution in the GNR, which depends self-consistently on the potential profile arising at the interface.

RESULTS AND DISCUSSION

As recently observed by Giovannetti *et al.*,[23] there are two possible adsorption schemes for graphene on metal surfaces: physisorption and chemisorption. The main differences between these two mechanisms are related to the magnitude of adsorption energy and the mixing of electronic states, where both are larger in the case of chemisorption. The projected density of states (PDOS) of carbon atoms shown in Figure 2 supports this description and allows one to clearly differentiate the weak physisorption on Au from the strong chemisorption on Ti. The case of Pd is a compromise between these two last cases; it is characterized by a relatively weak chemisorption, but the bonding involves a significant amount of hybridization, which can be associated with covalent bonding. The mixing between the d states of the metal and the π states of graphene is clearly observable in the PDOS diagram through a broadening of the energy levels of the pristine nanoribbon (Figure 2(a)) and a nonzero density of states in the band gap of the GNR when

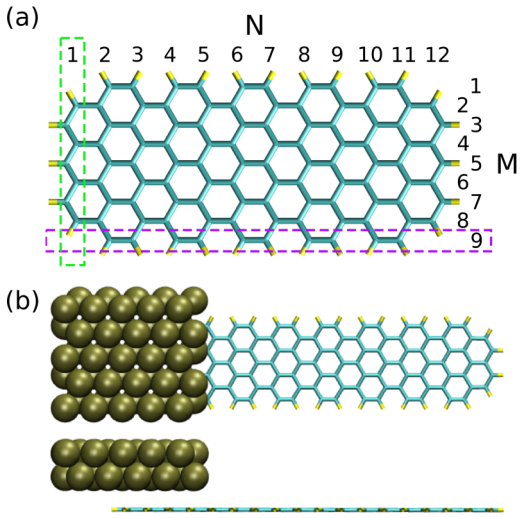

Figure 1. (a) 9 × 12 GNR illustrating the notation convention. (b) Typical GNR/contact system.

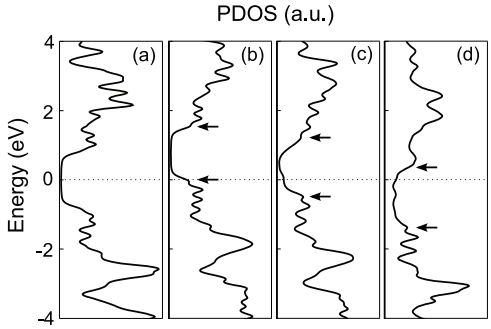

Figure 2. (a) DOS of a pristine 7 × 18 GNR. PDOS onto carbon atoms of the 7 × 18 GNR with (b) Au, (c) Pd, and (d) Ti contacts. σ = 0.2 eV. When needed for clarity, arrows indicate the limits of the valence and conduction band.

adsorbed on a Pd or Ti contact. The difference in bonding with the three metals studied is usually explained as a consequence of a high density of states (DOS) at the Fermi level for metals such as Ti due to an unfilled d band, as opposed to a low DOS of the valence s band of Au, while the Fermi level is near the edge of the d band for Pd.[24] As expected, chemisorption on Ti results in a large binding energy of ~0.4 eV per carbon atom as compared to 0.2 and 0.1 eV for Pd and Au, respectively. The equilibrium distances between the GNR and the metal surfaces follow a similar trend; a smaller distance is observed for Ti than for Pd and Au.

The mixing of states has a major impact on MIGS. Even though MIGS are present for all three metals studied, the high density of gap states with Ti, and to a lesser extent with Pd, gives rise to much more intense evanescent states in the graphene channel that could dramatically hinder the device operation. An example of such a state showing a clear evanescent decay away from the Ti contact is illustrated in Figure 3(a), which constitutes a first direct observation of MIGS enabled by the strong bonding with Ti. The presence of MIGS can be more easily revealed by calculating the local

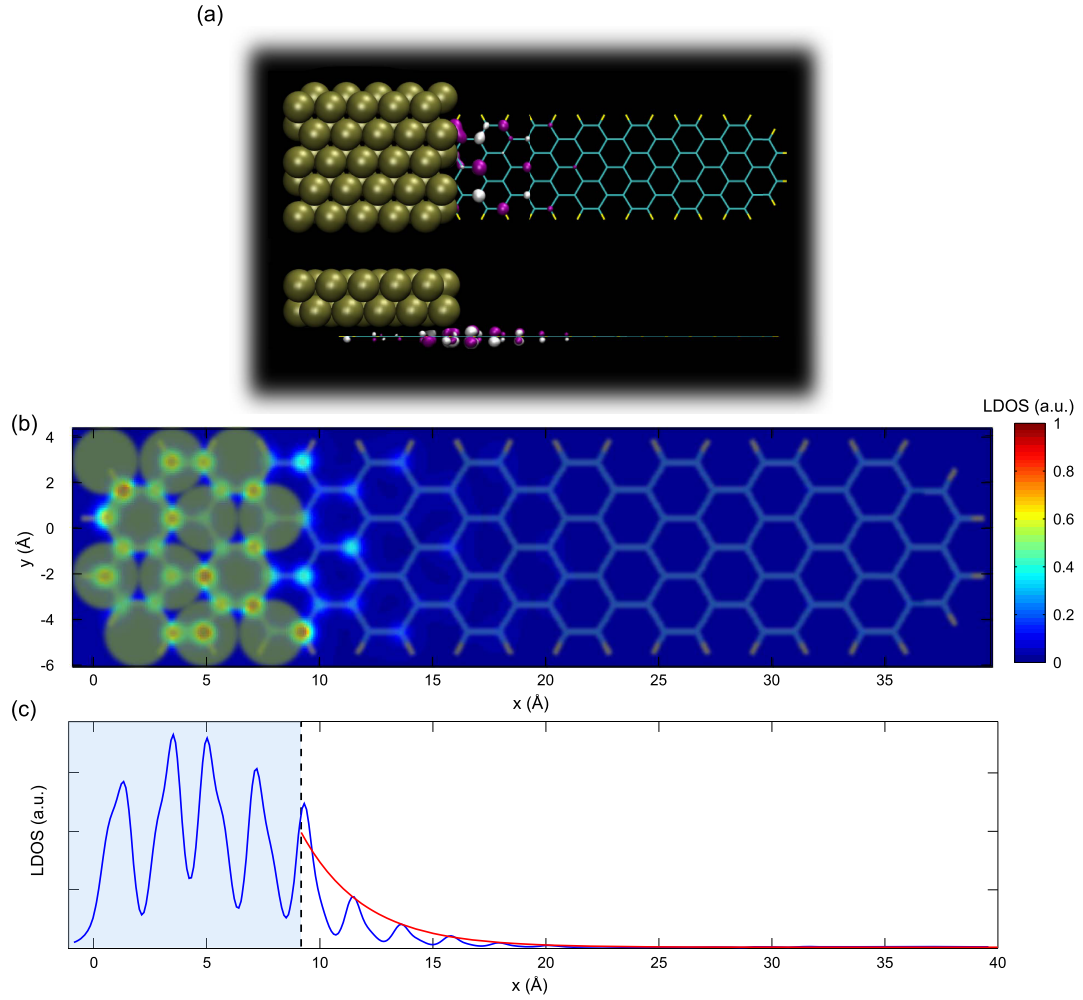

Figure 3. (a) MIGS wave function in the 7 × 18 GNR with a Ti contact with an isovalue of 0.03 Å$^{-3/2}$. (b) LDOS at Fermi energy in the 7 × 18 GNR with a Pd contact. Evaluated in a plane parallel to the GNR, 0.5 Å below with σ = 0.1 eV. (c) LDOS compressed along the ribbon's width. The contact is represented by the shaded area.

density of states (LDOS), which sums the contribution of multiple states in a small energy range due to the broadening introduced. Figure 3(b) shows the variation in LDOS at the Fermi level after adding a Pd contact. Similar LDOS have been obtained with the other metals. Mixing of states gives rise to high LDOS at the GNR/metal interface, but the immediate proximity of the metal cannot explain the slow decay into the channel. Integrating the LDOS along the ribbon's width results in the curve plotted in Figure 3(c). An exponential fit of the form $e^{-x/L}$ yields a decay length L of 2.8 Å. This exponential behavior is reminiscent of the MIGS' decay. This result suggests that MIGS could have a non-negligible effect up to 10 Å away from the GNR/metal interface, and hence a two-terminal device operated at low gate bias with a channel length smaller than 20 Å should not be operational due to a short circuit.

According to eq 1, Figure 4(a) shows that the decay length is not unique and strongly depends on the energy at which the LDOS is calculated for a GNR/Ti interface. As expected, the decay length L is minimal in the middle of the gap, but it increases as the energy approaches the edges of the valence or conduction bands delimited by the vertical lines in Figure 4(a). This quadratic dependence of L on E supports that the gap states originate directly from the GNR/metal interface. The theoretical curve (solid line) describing eq 1 is reported in Figure 4(a) for fixed values of E_g = 1.68 eV and a = 4.3 Å. Although this equation was derived for the case of a simple one-dimensional semiconductor, which does not consider the complex nature of the band structure of GNRs, the general agreement between our data points and the theoretical curve remains quite reasonable and reminds us that the extent of the MIGS in a practical device is highly bias-dependent.

In addition, the decay length is intimately related to the band-gap value, which depends on both the width and the length of the GNR. As the GNR elongates, the band gap (inset in Figure 4(b)) decreases and the decay length (calculated here in the middle of the gap) increases. As shown in Figure 4(b), L *vs* E_g follows an

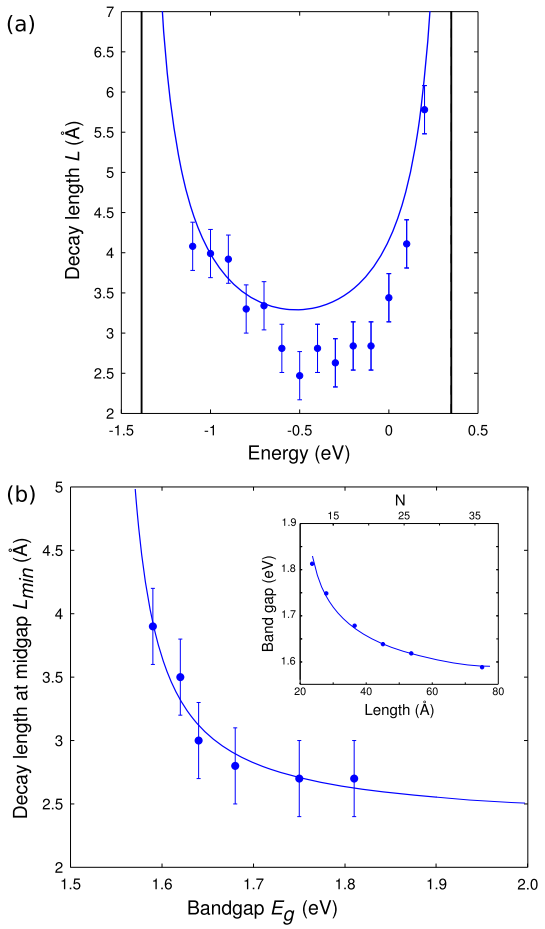

Figure 4. (a) Decay length as a function of the MIGS' energy in the 7 × 18 GNR with a Ti contact. (b) MIGS decay length at mid gap as a function of band gap in 7 × *N* GNRs with a Pd contact. Inset: Bandgap as a function of length in pristine 7 × *N* GNRs.

inverse relation as expected, though not the one given in eq 2, once again because of the complexity of GNRs' band structure. For GNRs with a width of $M = 7$, we find a simple relation (eq 3) between the decay length and the band gap that can be easily applied experimentally to estimate the critical length of a device.

$$L_{\min}[\text{nm}] = \frac{0.077}{E_g[\text{eV}] - 1.54} + 2.3 \qquad (3)$$

By comparing GNRs with different widths *W*, the results in Table 1 confirm that the MIGS decay length once again strongly depends on the band gap. The smaller the band gap, the larger the penetration. The minimum decay length even reaches the significant extent of 5.6 Å for the small band gap 9 × 18 GNR, which reiterates the possibly catastrophic effect of MIGS in electronic devices. Note that the 8 × 18 GNR has here been omitted because of its metallic character. The results in Table 1 do not follow eq 3 because the latter applies only to GNRs belonging to the 7 × *N* family. Effectively, we can expect the MIGS dispersion relation to differ significantly for GNRs with different

TABLE 1. Band Gap and MIGS Decay Length at Mid Gap for *M* × 18 GNRs with a Pd Contact

GNR	*W* (Å)	E_g (eV)	L_{min} (Å)
6 × 18	6.2	1.43	4.8
7 × 18	7.4	1.68	2.8
9 × 18	9.9	1.09	5.6

widths because of their dissimilar electronic structures. Armchair GNRs with slightly increasing width are known for displaying large band-gap oscillations with a 3-fold periodicity.[2,3] Hence, for ribbons in the nanoscale, MIGS penetration primarily depends on the band gap, and due to quantum effects, it cannot simply be expressed as a function of the width of the GNR. Only when looking at the problem from a macroscopic angle for which $E_g \propto 1/W$[1,25] can the proportionality between decay length and width be established as reported by Golizadeh-Mojarad and Datta.[16]

By calculating the LDOS at different energies, we can visualize the band diagram along the device as shown in Figure 5 for a GNR/Pd system. Note that MIGS with a decreasing penetration length toward the middle of the gap can be seen on the right side of the contact. In this case, the higher density of MIGS below the Fermi energy suggests an asymmetric behavior under an applied gate field as mentioned by Rochefort *et al.*[26] for carbon nanotubes, meaning that a negatively biased gate would be less effective in switching. This particular effect strongly depends on the electronic structure of the metal that defines the Fermi level and the density of MIGS.

Like any other electronic states, MIGS can hold charges that depend on the position of the Fermi level relative to the charge neutrality point (CNP), which is generally assumed to be located at mid gap, where the contributions from the valence and conduction bands are of the same order. More precisely, occupied (respectively unoccupied) states above (respectively below) the CNP translate to a negative (respectively positive) net charge.[19] Since MIGS have an evanescent form, a similar behavior can be expected from the charge distribution. Figure 6(a,b) show the differential charge density ($\Delta\rho = \rho_{GNR/M} - \rho_{GNR} - \rho_M$) in a 7 × 18 GNR physisorbed on a Au contact. The red (blue) region indicates an increase (decrease) in electron density after introducing the metal contact. Charge transfer is more important at the GNR/metal interface and slowly decays into the GNR channel. Löwdin population analysis was used to estimate the variation of charge on each carbon atom in the GNR after its adsorption on the metal contact. The result of this analysis is reported in Figure 6(c) and mainly shows that the accumulated positive charge in the GNR is quite significant near the Au contact but rapidly decreases away from the GNR/Au interface. An exponential fit of the decrease in accumulated charge in the GNR away from the Au

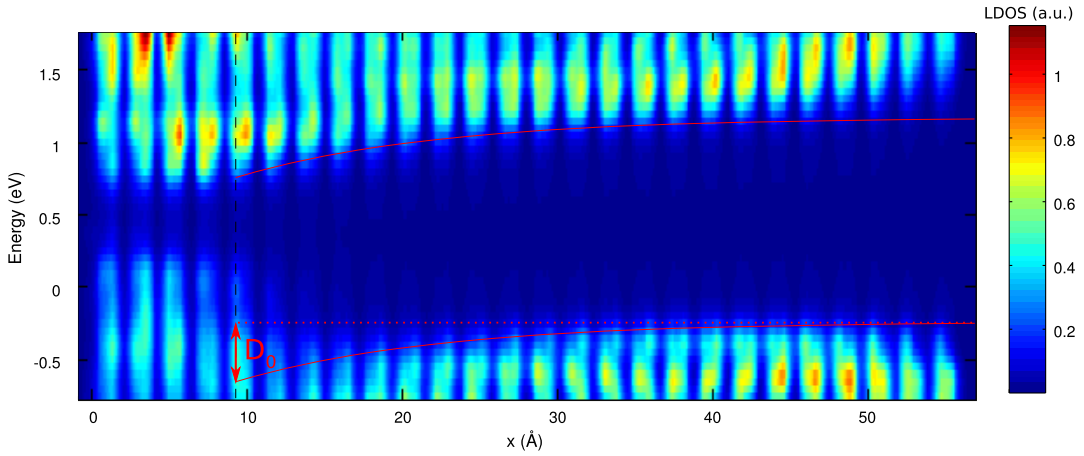

Figure 5. LDOS as a function of *x* and energy (with the Fermi level set to 0 eV) in the 7 × 26 GNR with a Pd contact. Evaluated in a plane parallel to the GNR, 0.5 Å below with $\sigma = 0.2$ eV. The vertical dashed line indicates the limit of the contact located on the left. Red curves represent the electrostatic potential in the GNR.

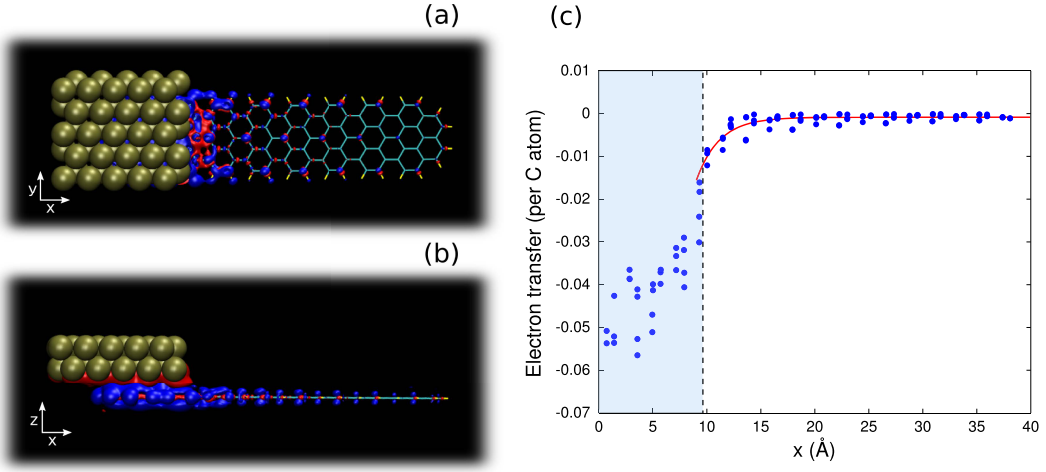

Figure 6. Differential electronic density in the 7 × 18 GNR with a Au contact viewed (a) from above and (b) from the side. Positive/negative in red/blue with an isovalue of ±0.001 Å^{-3}. (c) Löwdin electron transfer per carbon atom. The contact is represented by the shaded area.

contact gives a decay length of $L = 2.2$ Å (red curve). If this positive charge is effectively associated with the MIGS located between the Fermi level and the middle of the gap, it should be equivalent to the value obtained by the integration of the LDOS over this energy range, which for a Au contact gives a decay length of 2.6 Å. Taking into account the error on the fit, mostly due to the fact that the charge is estimated from a sum of different exponentials instead of a single one and also to errors inherent to the population analysis, this last value (2.6 ± 0.3 Å) agrees well with the value estimated from the Löwdin analysis (2.2 ± 0.3 Å), supporting the presence of MIGS.

Now that the relation between MIGS and charge transfer has been evidenced, one might wonder what actually sets the position of the Fermi level, which is responsible for populating the MIGS, relative to the GNR's bands. As for any metal/semiconductor interface, band lineup depends on both materials' properties as well as on the interface dipole, as shown in Figure 7. Knowing the charge distribution in the

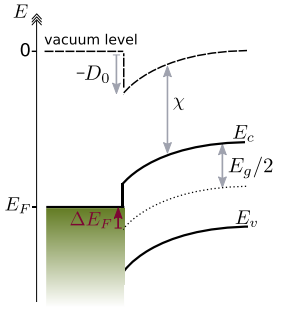

Figure 7. Schematic band lineup at the GNR/metal interface.

system, the latter can be estimated by calculating the electrostatic potential profile in the junction. Note that as opposed to planar bulk junctions invariant in the direction parallel to the interface, low-dimensional systems are characterized by a potential varying in all three dimensions of space.[27,28] Since the potential diverges at the nuclei, the only way to evaluate it in the plane of the GNR is to neglect a nucleus's contribution

past a certain cutoff radius. After subtracting the pristine GNR's contribution, this yields the curves superposed in Figure 5. This representation confirms the expected result that the band curvature, extending over a few nm, is dictated by the potential in the junction, which goes to zero at the end of the GNR. More importantly, the potential profile allows us to evaluate the height of the dipole D_0 at the interface, which determines the band lineup based on eq 4:

$$\Delta E_F = E_F + \chi + \frac{E_g}{2} - D_0 \quad (4)$$

where χ and E_g are the pristine GNR's electronic affinity and band gap, E_F is the Fermi energy of the GNR/metal complex (which would converge toward minus the metal's work function for an extended electrode), and ΔE_F is the Fermi level's displacement from mid gap at the junction. The latter can also be estimated from the band diagram. Table 2 compares the Fermi level's displacements obtained using both methods for the three metals with excellent agreement. The dipole derived from the charge distribution thus effectively sets the Fermi level. Moreover, as discussed previously, MIGS' occupation is responsible for the evanescent charge distribution in the channel and that effectively closes the loop. In that sense, the intricate relation between MIGS, charge transfer, and electrostatics has now been clarified. However, it is important to stress that all three are interdependent and cannot be assessed independently.

TABLE 2. Fermi Level Displacement As Obtained from eq 4 ($\Delta E_F^{(1)}$) and from Band Diagrams ($\Delta E_F^{(2)}$) at the 7 × 18 GNR/Metal Interface (E_g = 1.68 eV, χ = 2.96 eV)

	E_F (eV)	D_0 (eV)	$\Delta E_F^{(1)}$ (eV)	$\Delta E_F^{(2)}$ (eV)
Au	−4.85	−0.50 ± 0.05	−0.55 ± 0.05	−0.50 ± 0.05
Pd	−4.35	−0.50 ± 0.05	−0.05 ± 0.05	0.00 ± 0.05
Ti	−3.28	0.05 ± 0.05	0.47 ± 0.05	0.50 ± 0.05

CONCLUSIONS

We have performed DFT calculations on finite graphene nanoribbons with Au, Pd, and Ti contacts, thus covering a wide range of binding interactions, from physisorption (for Au) to chemisorption (for Ti). Attention is focused on MIGS, which limit the miniaturization of GNR-based devices to channels a few nanometers long according to the decay length calculated. This parameter is closely related to the band gap, which could be used as a simple guide for device engineering. MIGS must be treated carefully for metals such as Ti strongly bonding with graphene since hybridization leads to a higher density of MIGS. In fact, MIGS, binding, charge transfer, and electrostatics are all interconnected. Charge transfer is responsible for the three-dimensional potential profile in the junction that governs band alignment and thus the population in the MIGS, and this in turn results in the long-range part of the charge transfer. For this reason, graphene/metal interfaces are nontrivial and need to be treated self-consistently.

METHODS

The DFT calculations were carried out at zero temperature with the NWChem package[29] within the generalized gradient approximation using the PBE functional.[30] On the basis of comparative calculations carried out by Barone *et al.*,[31] PBE accurately renders the band-gap oscillations in GNRs even though it slightly underestimates the band gap. Nevertheless, this should have no effect on the general interpretation of our results. The 3-21G* and LANL2DZ (with corresponding pseudopotentials) basis sets were used for the GNR and the metallic contacts, respectively. Although the size of the basis sets is limited, the variation in the results obtained for the three different metals is sufficiently large for basis sets to have a minimal impact on our final conclusions. Nevertheless, we have also performed a few additional calculations with more complete basis sets for GNRs without noticing a significant variation in the results.

The top contact electrodes were modeled by a metallic cluster made of two atomic layers containing at least 25 atoms each and where the atomic positions were fixed at the bulk lattice value. The more important result at this stage is that such electrode geometry leads to a correct DOS diagram for the metal. An increasing width or number of atomic planes in the metal cluster had no qualitative effects on the electronic structure properties. Moreover, to verify the correctness of our single contact geometry, a calculation was carried out using two titanium contacts with a minimal basis set. As expected, the decay length obtained at each electrode agrees with that found in a comparable system with a single contact such that the second contact can be omitted without loss of generality.

Our electronic structure calculations were carried out as follow. First, the geometry of the isolated nanoribbon, uniformly saturated by hydrogen atoms, was fully optimized. The distance between the metal cluster and a typical GNR was then optimized, while maintaining a fixed geometry for the GNR. This assumption was considered in order to simulate and study the behavior of a flat GNR system, exempt from any corrugation that could be induced both by the contacts and by the substrate but that would necessitate larger models to be accurately described. The relative orientation of the GNR on the surface reproduces the stable configuration previously calculated by DFT for graphene on similar metals.[23,32] We found that the 7 × 12 GNR is adsorbed at 3.32, 2.40, and 2.19 Å over Au, Pd, and Ti surfaces, respectively, confirming that the level of theory used efficiently reproduces the results previously published for 2D graphene.[24,32,33]

The DOS diagrams were generated by broadening the discrete energy levels (of energy ε_i) of the system with a Gaussian−Lorentzian function G such that

$$\mathrm{DOS}(E) = \sum_i \delta(E - \varepsilon_i) G(E - \varepsilon_i) \quad (5)$$

where

$$G(E - \varepsilon_i) = \frac{\sqrt{2/\pi}}{\sigma} \exp\left(-2\frac{(E-\varepsilon_i)^2}{\sigma^2}\right) + \frac{2\sigma}{\pi(\sigma^2 + 4(E-\varepsilon_i)^2)}$$

The PDOS onto a given atomic orbital φ_μ in a nonorthogonal basis set is defined as[34]

$$\mathrm{PDOS}_\mu(E) = \sum_i \sum_\nu c_\mu^{(i)*} c_\nu^{(i)} S_{\mu\nu} \delta(E - \varepsilon_i) G(E - \varepsilon_i) \quad (6)$$

where

$$S_{\mu\nu} = \langle \phi_\mu | \phi_\nu \rangle$$

for normalized molecular orbitals of the form:

$$\psi_i(\vec{r}) = \sum_{\mu} c_{\mu}^{(i)} \phi_{\mu}(\vec{r}) \quad (7)$$

The LDOS has also been computed, using

$$\mathrm{LDOS}(\vec{r}, E) = \sum_{i} |\psi_i(\vec{r})|^2 \delta(E - \varepsilon_i) G(E - \varepsilon_i) \quad (8)$$

Conflict of Interest: The authors declare no competing financial interest.

Acknowledgment. This work was supported by the Natural Sciences and Engineering Research Council of Canada (NSERC), and Ministère du Développement économique, de l'Innovation et de l'Exportation (MDEIE) through the PSR-SIIRI program. Computational resources were provided by the Calcul Québec and Compute Canada. Chloé Archambault is also grateful to the NSERC for financial support.

REFERENCES AND NOTES

1. Han, M. Y.; Özyilmaz, B.; Zhang, Y.; Kim, P. Energy Band-Gap Engineering of Graphene Nanoribbons. *Phys. Rev. Lett.* **2007**, *98*, 206805.
2. Nakada, K.; Fujita, M.; Dresselhaus, G.; Dresselhaus, M. S. Edge State in Graphene Ribbons: Nanometer Size Effect and Edge Shape Dependence. *Phys. Rev. B* **1996**, *54*, 17954–17961.
3. Son, Y.-W.; Cohen, M. L.; Louie, S. G. Energy Gaps in Graphene Nanoribbons. *Phys. Rev. Lett.* **2006**, *97*, 216803.
4. Cai, J.; Ruffieux, P.; Jaafar, R.; Bieri, M.; Braun, T.; Blankenburg, S.; Muoth, M.; Seitsonen, A. P.; Saleh, M.; Feng, X.; *et al.* Atomically Precise Bottom-Up Fabrication of Graphene Nanoribbons. *Nature* **2010**, *466*, 470–473.
5. Li, X.; Wang, X.; Zhang, L.; Lee, S.; Dai, H. Chemically Derived, Ultrasmooth Graphene Nanoribbon Semiconductors. *Science* **2008**, *319*, 1229–1232.
6. Wang, X.; Dai, H. Etching and Narrowing of Graphene from the Edges. *Nat. Chem.* **2010**, *2*, 661–665.
7. Jiao, L.; Wang, X.; Diankov, G.; Wang, H.; Dai, H. Facile Synthesis of High-Quality Graphene Nanoribbons. *Nat. Nanotechnol.* **2010**, *5*, 321–325.
8. Liao, L.; Bai, J.; Cheng, R.; Lin, Y.-C.; Jiang, S.; Huang, Y.; Duan, X. Top-Gated Graphene Nanoribbon Transistors with Ultrathin High-k Dielectrics. *Nano Lett.* **2010**, *10*, 1917–1921.
9. Schwierz, F. Graphene Transistors. *Nat. Nanotechnol.* **2010**, *5*, 487–496.
10. Streetman, B. G.; Banerjee, S. K. *Solid State Electronic Devices*, 6th ed.; Pearson Prentice Hall: Upper Saddle River, NJ, 2006; p 581.
11. Blake, P.; Yang, R.; Morozov, S. V.; Schedin, F.; Ponomarenko, L. A.; Zhukov, A. A.; Nair, R. R.; Grigorieva, I. V.; Novoselov, K. S.; Geim, A. K. Influence of Metal Contacts and Charge Inhomogeneity on Transport Properties of Graphene Near the Neutrality Point. *Solid State Commun.* **2009**, *149*, 1068–1071.
12. Mueller, T.; Xia, F.; Freitag, M.; Tsang, J.; Avouris, P. Role of Contacts in Graphene Transistors: A Scanning Photocurrent Study. *Phys. Rev. B* **2009**, *79*, 245430.
13. Lee, E. J. H.; Balasubramanian, K.; Weitz, R. T.; Burghard, M.; Kern, K. Contact and Edge Effects in Graphene Devices. *Nat. Nanotechnol.* **2008**, *3*, 486–490.
14. Xia, F.; Mueller, T.; Golizadeh-Mojarad, R.; Freitag, M.; Lin, Y.-m.; Tsang, J.; Perebeinos, V.; Avouris, P. Photocurrent Imaging and Efficient Photon Detection in a Graphene Transistor. *Nano Lett.* **2009**, *9*, 1039–1044.
15. Liang, G.; Neophytou, N.; Lundstrom, M. S.; Nikonov, D. E. Contact Effects in Graphene Nanoribbon Transistors. *Nano Lett.* **2008**, *8*, 1819–1824.
16. Golizadeh-Mojarad, R.; Datta, S. Effect of Contact Induced States on Minimum Conductivity in Graphene. *Phys. Rev. B* **2009**, *79*, 085410.
17. Barraza-Lopez, S.; Vanević, M.; Kindermann, M.; Chou, M. Y. Effects of Metallic Contacts on Electron Transport through Graphene. *Phys. Rev. Lett.* **2010**, *104*, 076807.
18. Deretzis, I.; Fiori, G.; Iannaccone, G.; La Magna, A. Atomistic Quantum Transport Modeling of Metal-Graphene Nanoribbon Heterojunctions. *Phys. Rev. B* **2010**, *82*, 161413(R).
19. Mönch, W. *Semiconductor Surfaces and Interfaces*, 2nd ed.; Springer-Verlag: Berlin, 1995; p 442.
20. García-Moliner, F.; Flores, F. *Introduction to the Theory of Solid Surfaces*; Cambridge University Press: Cambridge, 1979; p 437.
21. Hod, O.; Peralta, J. E.; Scuseria, G. E. Edge Effects in Finite Elongated Graphene Nanoribbons. *Phys. Rev. B* **2007**, *76*, 233401.
22. Shemella, P.; Zhang, Y.; Mailman, M.; Ajayan, P. M.; Nayak, S. K. Energy Gaps in Zero-Dimensional Graphene Nanoribbons. *Appl. Phys. Lett.* **2007**, *91*, 042101.
23. Giovannetti, G.; Khomyakov, P. A.; Brocks, G.; Karpan, V. M.; van den Brink, J.; Kelly, P. J. Doping Graphene with Metal Contacts. *Phys. Rev. Lett.* **2008**, *101*, 026803.
24. Ran, Q.; Gao, M.; Guan, X.; Wang, Y.; Yu, Z. First-Principles Investigation on Bonding Formation and Electronic Structure of Metal-Graphene Contacts. *Appl. Phys. Lett.* **2009**, *94*, 103511.
25. Wakabayashi, K.; Fujita, M.; Ajiki, H.; Sigrist, M. Electronic and Magnetic Properties of Nanographite Ribbons. *Phys. Rev. B* **1999**, *59*, 8271–8282.
26. Rochefort, A.; Di Ventra, M.; Avouris, P. Switching Behavior of Semiconducting Carbon Nanotubes under an External Electric Field. *Appl. Phys. Lett.* **2001**, *78*, 2521–2523.
27. Xue, Y.; Ratner, M. A. Scaling Analysis of Schottky Barriers at Metal-Embedded Semiconducting Carbon Nanotube Interfaces. *Phys. Rev. B* **2004**, *69*, 161402.
28. Heimel, G.; Salzmann, I.; Duhm, S.; Koch, N. Design of Organic Semiconductors from Molecular Electrostatics. *Chem. Mater.* **2011**, *23*, 359–377.
29. Valiev, M.; Bylaska, E.; Govind, N.; Kowalski, K.; Straatsma, T.; Van Dam, H.; Wang, D.; Nieplocha, J.; Apra, E.; Windus, T.; *et al.* NWChem: A Comprehensive and Scalable Open-Source Solution for Large Scale Molecular Simulations. *Comput. Phys. Commun.* **2010**, *181*, 1477–1489.
30. Perdew, J.; Burke, K.; Ernzerhof, M. Generalized Gradient Approximation Made Simple. *Phys. Rev. Lett.* **1996**, *77*, 3865–3868.
31. Barone, V.; Hod, O.; Peralta, J. E.; Scuseria, G. E. Accurate Prediction of the Electronic Properties of Low-Dimensional Graphene Derivatives Using a Screened Hybrid Density Functional. *Acc. Chem. Res.* **2011**, *44*, 269–279.
32. Gong, C.; Lee, G.; Shan, B.; Vogel, E. M.; Wallace, R. M.; Cho, K. First-Principles Study of Metal−Graphene Interfaces. *J. Appl. Phys.* **2010**, *108*, 123711.
33. Khomyakov, P. A.; Giovannetti, G.; Rusu, P. C.; Brocks, G.; van den Brink, J.; Kelly, P. J. First-Principles Study of the Interaction and Charge Transfer between Graphene and Metals. *Phys. Rev. B* **2009**, *79*, 195425.
34. Fassaert, D. J. M.; Van der Avoird, A. LCAO Studies of Hydrogen Chemisorption on Nickel: I. Tight-Binding Calculations for Adsorption on Periodic Surfaces. *Surf. Sci.* **1976**, *55*, 291–312.